JTTEE5 10:83-93

Particle Melting Behavior during High-Velocity Oxygen Fuel Thermal Spraying

J. He, M. Ice, and E. Lavernia

(Submitted 13 January 2000; in revised form 2 March 2000)

Particle melting behavior during high-velocity oxygen fuel (HVOF) thermal spraying was investigated using Inconel 625 powders. The powder characteristics and coating properties were investigated using scanning electron microscopy (SEM), x-ray, and microhardness studies. Results indicated that the volume fraction of unmelted particles in the coatings was dependent on the proportion of powder within a specified size range, in these experiments, 30 to 50 μm. This particle size range was primarily determined by the particle temperature, which was measured during spraying. Particle temperature significantly decreased as particle size increased. The microhardness values for the coatings containing unmelted particles were predicted by a simple rule-of-mixtures equation for the case of a low volume fraction of unmelted particles. However, for the condition of high volume fraction of unmelted particles, the measured microhardness values did not compare favorably with the calculated values, probably due to the presence of porosity, which occurred in the form of voids found among unmelted particles. The microstructure and characteristics of the feedstock powder were retained in the corresponding coating under certain spray conditions.

Keywords coatings, HVOF, Inconel 625, grain size, microstructure

1. Introduction

High-velocity oxygen fuel (HVOF) spraying is widely regarded as the most significant development in the thermal spray industry since the development of plasma spray.[1] High-velocity oxygen fuel is characterized by a high particle velocity and a low flame temperature when compared to plasma spraying. Using an internal combustion jet fuel (propylene, acetylene, propane, and hydrogen gases), HVOF generates a supersonic gas velocity of 1830 m/s. During spraying, powder particles are rapidly heated and accelerated onto substrate at a rate of 600 to 800 m/s, compared to plasma particle velocity, which is typically 200 m/s.[2–4] Many excellent investigations on HVOF have been published in recent years.[5–9] Through a combination of HVOF technology and mechanical milling, a process that allows for production of nanostructured feedstock powders, several nanostructured coatings have been successfully sprayed.[11–14] Why nanostructured feedstock powders maintain their initial structure, after a transition into a completely molten state, is an area of research currently under investigation. Unmelted particles have been observed in Inconel 718 (INCO Alloys International, Huntington, WV),[3] NiCr[15] metallic coatings, and Cr_3C_2/NiCr[13] and WC-12% Co[14] coatings. However, because HVOF spraying parameters were originally developed on the basis of liquid droplets impacting on a substrate,[1,10] the microstructure and properties associated with unmelted particles have not yet been investigated. Microstructure characterization, such as change in grain size, in unmelted particles will help provide an understanding of issues surrounding nanostructured coating formation. Experiments conducted on Inconel 625 coatings[2,10] were carried out because of the importance of this alloy in the aerospace industry. However, in these studies, propylene gas was used as the thermal spray fuel as opposed to hydrogen because of its ability to produce 100 K higher flame temperature than hydrogen.[10] Moreover, using hydrogen as fuel, a finer and denser microstructure was obtained in a NiCr coating.[15] Therefore, the primary objective of the present study is to investigate the microstructure and properties of Inconel 625 coatings, paying particular attention to the influence that particle melting has on both microstructure and properties. In the present study, hydrogen is used as fuel and factory recommended spraying parameters are employed. The influence of feedstock powder particle size on particle temperature, volume fraction of unmelted particles, and the properties of Inconel 625 coatings is investigated in detail.

J. He, M. Ice, and **E. Lavernia,** Department of Chemical and Biochemical Engineering and Materials Science, University of California, Irvine, Irvine, CA 92697-2575. Contact e-mail: lavernia@uci.edu.

Experimental Procedure

2.1. Materials

Commercially available gas-atomized Inconel 625 powder (Diamalloy 1005 Amdry 625 (Sulzer Metco Inc., Westbury, NY)), with a nominal particle size of (–45 + 11) μm, was used in the present study. On the basis of ASTM E 1019 and ASTM E 1097 standards, chemical analysis of the as-received powder was conducted by Luvak Inc., a professional chemical analysis company located in Boylston, MA. The results of chemical analysis on the powder are shown in Table 1.

2.2 Powder Characterization

The as-received powder was separated into different particle sizes by mechanical sieving. The particle size and distribution were determined using a Coulter LS particle size analyzer, made by Coulter Co. (Miami, FL). X-ray diffraction measurements con-

Table 1 Chemical composition of Inconel 625 powder (wt.%)

Ni	Cr	Mo	Nb	Fe	Ti	Al	C	N	O
66.5	20.6	8.99	3.55	0.045	0.012	0.24	0.006	0.075	0.015

Table 2 Spraying parameters used to produce Inconel coatings

Gas	Pressure (MPa)	FMR (a)	GSFR (b)	Parameter	Setting
Air	0.69	44	6182	Powder feed rate	0.315 g/s
Fuel	0.965	62	11405	X-Y traverse speed	1.016 m/s
Nitrogen	1.034	55	220	Spraying distance	0.203 m
Oxygen	1.17	32	3846	. . .	. . .

(a) FMR: flow meter reading
(b) GSFR: gas standard flow rate (cm^3/s)

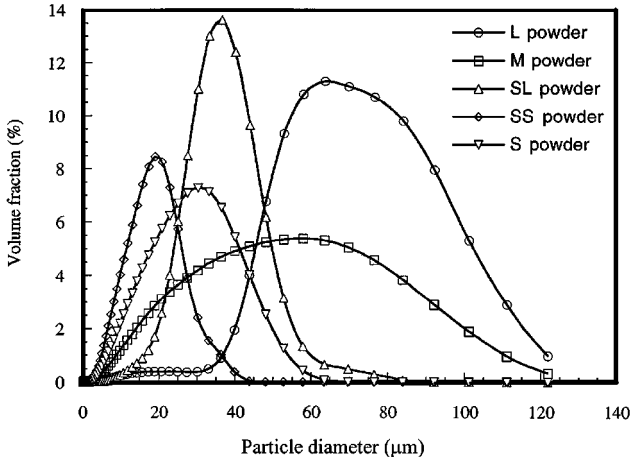

Fig. 1 Inconel 625 particle size distribution curves

ducted on the powders were carried out using a Siemens (Erlangen, Germany) D5000 diffractometer equipped with a graphite monochromator using Mo $K_a(\lambda = 0.070923$ nm) radiation. A low scanning rate of 0.12°/min was used to guarantee the accuracy of the measurements. Scanning electron microscopy (SEM) analysis on the morphology of the powder samples was conducted on a Philips XL 30 FEG microscope (Philips Electronic Instruments Corp., Mahwah, NJ). Cross sections of the powder particles were prepared by mounting the particles in conductive carbon powder, rather than traditional resin, to enhance electrical conductivity; this was followed by grinding and mechanical polishing. Thermal analysis conducted on the as-received powder was conducted using a Perkin-Elmer (Norwalk, CT) DTA 7 differential thermal analyzer (DTA).

2.3 HVOF Thermal Spraying

To prepare Inconel 625 coatings, a Sulzer Metco Diamond Jet HVOF thermal spray facility was used. The main constituents of this facility are described in detail elsewhere.[13,14] With the "in-flight" particle pyrometer IPP-2010 and torch diagnostic system TDS-1610, manufactured by In-Flight Ltd. Co. (Idaho Falls, ID), accurate average particle temperatures can be measured as well as trajectory and particle flow characteristics. The in-flight particle pyrometer is designed to detect changes in temperature based on the emissivity of light expelled from the particles as they traverse from the barrel of the gun to the substrate. The pyrometer interfaces with the torch diagnostic system directly; a light emitting diode (LED) is involved to guarantee alignment of the pyrometer with the center of the flame. When the cable is placed in the alignment port, light is emitted from the end of the pyrometer to shine on the center line of the flame. Infrared rays radiated from the particles, not the flame, are transmitted by a fused fiber coupler to two infrared detectors of different spectral sensitivity. A value for the particle temperature is obtained by calculating the ratio of the output voltage from these two detectors. Two color pyrometer systems are used in many applications where temperature measurements are needed, but the use or placement of a thermocouple is not applicable or available.[16,17] The Diamond Jet (Sulzer Metco Inc., Westbury, NY) brings in oxygen, air, and fuel, in these experiments, hydrogen, from the Diamond Jet Controller (DJC) into the rear of the gun in the proper stoichiometric ratio. This gaseous mixture is ignited by an arc current creating a supersonic, low-temperature flame with gas velocities of 1830 m/s and temperatures around 2200 K. From a 9 MP hopper powder feed unit, nitrogen carrier gas brings the powder into the rear of the gun and then axially into the flame. The powder is heated in the gun barrel, which was installed on a "Parker" (Sulzer Metco Inc., Westbury, NY) automated X-Y system operating at a traverse velocity of 1.016 m/s and then sprayed onto a mild steel substrate. The spraying parameters are summarized in Table 2.

Table 3 Particle diameter and size range of Inconel 625 powder used in this study

Code	SS	S	SL	M	L
Average diameter (μm)	17.01	26.71	36.02	44.96	69.97
10% less than (μm)	7.39	9.58	22.91	12.90	44.77
25% less than (μm)	11.20	15.54	29.05	22.87	55.52
50% less than (μm)	16.59	24.41	35.69	40.52	68.97
75% less than (μm)	22.07	34.10	42.66	63.38	85.54
90% less than (μm)	27.08	42.45	49.58	83.98	100.20

2.4 Coating Characterization

For SEM observation, samples were cut from the transverse section of the coatings, mounted in conductive carbon powder, and then prepared by standard metallographic procedures, however, without using electric polishing or chemical etching. The cross section of the coatings was examined using a Philips XL 30 FEG scanning electron microscope in either backscattered electron (BSE) or secondary electron (SE) mode. The microhardness was tested on a Buehler Micromet 2004 (Lake Bluff, IL) microhardness tester using a load of either 100 or 300 g. Each microhardness value was obtained from an average value of 30 tests.

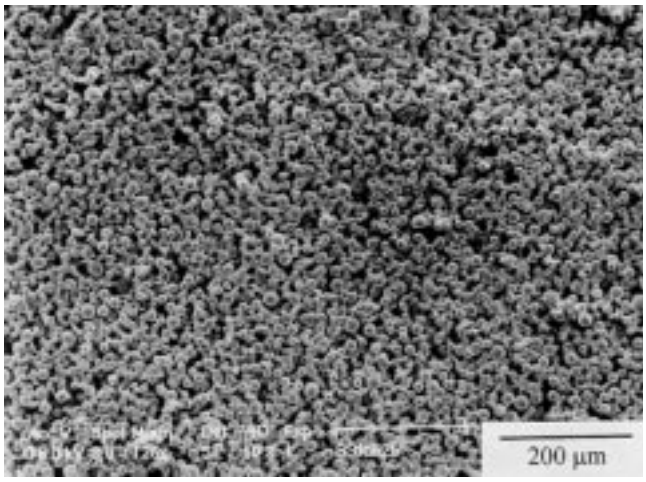

(a)

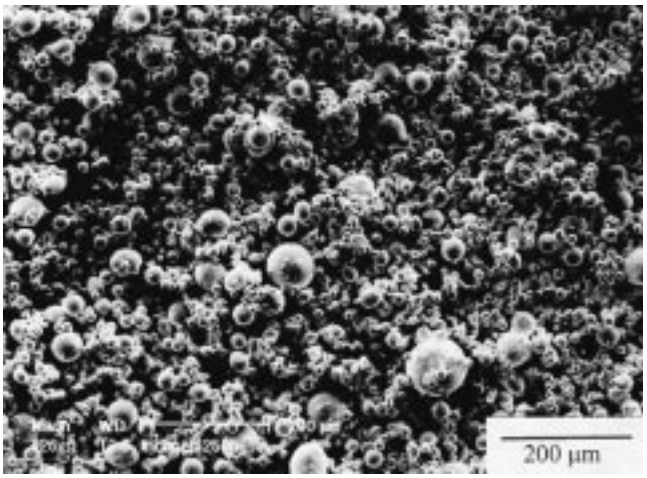

(d)

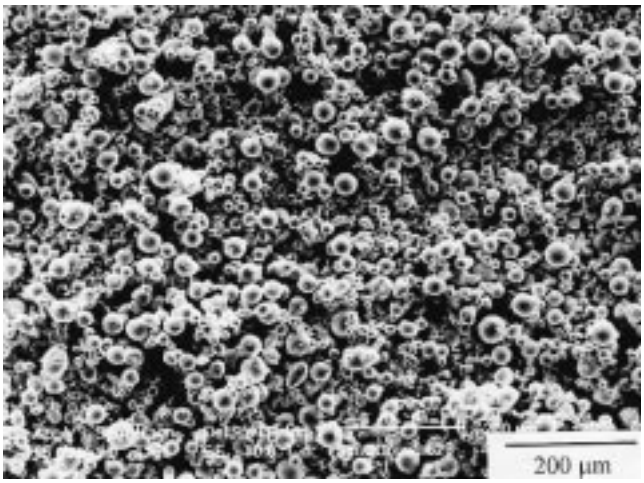

(b)

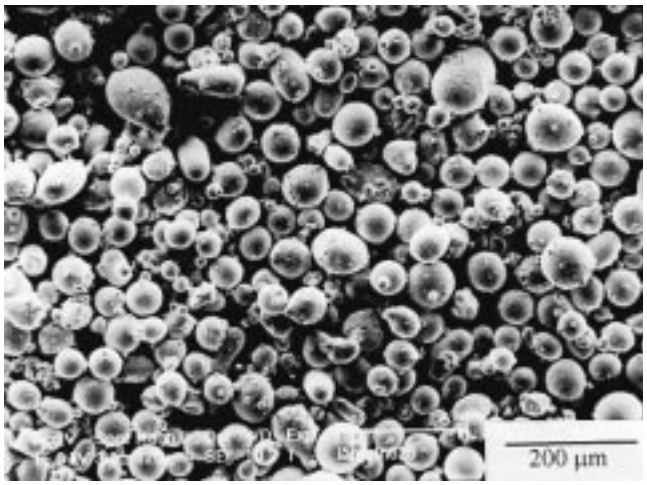

(e)

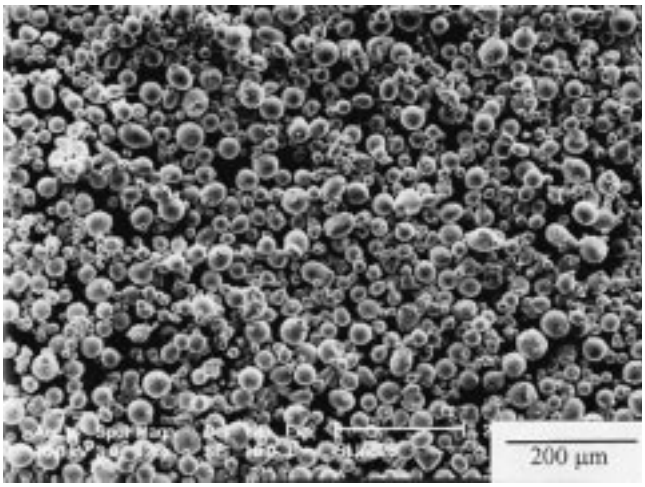

(c)

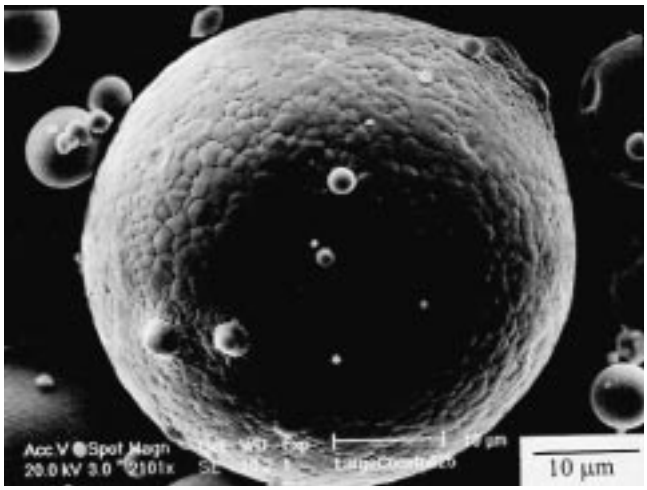

(f)

Fig. 2 Morphology of Inconel 625 powders used. **(a)** SS powder, **(b)** S powder, **(c)** SL powder, **(d)** M powder, **(e)** L powder, and **(f)** a detailed view of a particle, (equiaxed structures are visible on the external surface)

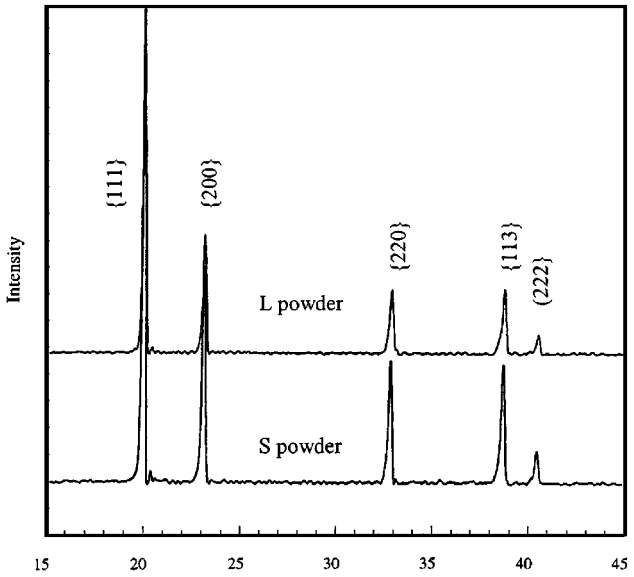

Fig. 3 XRD spectra of Inconel 625 powders

3. Results and Discussion

3.1 Powder Characteristics

The as-received powder, designated hereafter as M powder, was separated into different size ranges with two particle sizes by mechanically sieving, the larger one labeled L powder and the smaller one labeled S powder. The S powder was separated once again using a sieve with higher mesh number (500); the larger one was labeled as SL powder and the smaller one as SS powder. The average particle sizes (in diameter) and size range of these five powders are listed in Table 3. The "10% less than" in the table means that 10 vol.% of particle diameters are less than the values listed in the table, and "25%, 50%, 75%, and 90% less than" means the same. Distribution curves of particle sizes are plotted in Fig. 1. The M powder includes all particles in SS, S, SL, and L powder, because these powders were separated from M powder.

The morphology of these powders is shown in Fig. 2(a) to (e). All particles are near spheroidal and the morphology is size independent, although some small particles exist in the form of satellites attached to larger particles. The observed particle morphology is consistent with the characteristics that are typical of gas atomization. Particle sizes observed on SEM micrographs are in agreement with the results from the particle size analyzer shown in Table 3 and Fig. 1. A detailed view of a particle is also shown in Fig. 2(f); an equiaxed grain structure is visible on the external surfaces of majority particles, although dendritic structures are occasionally observed on the external surfaces of a few particles.

X-ray diffraction (XRD) spectra of the powders are shown in Fig. 3. The observed XRD peaks are {111}, {200}, {220}, {113}, and {222} peaks of a fcc structure material with an average lattice constant of 0.3585 nm. There were either no second phases, detected by the XRD analysis, or the volume fractions of any secondary phases were lower than the limitation of x-ray detection (usually, 5%). Phase constitution of the powders is independent of particle size. Powders with different particle sizes have the same full-width at half-maximum values in XRD; thus,

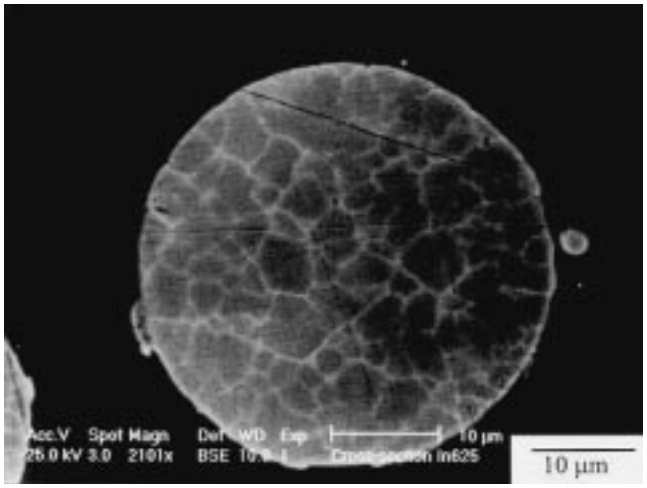

(a)

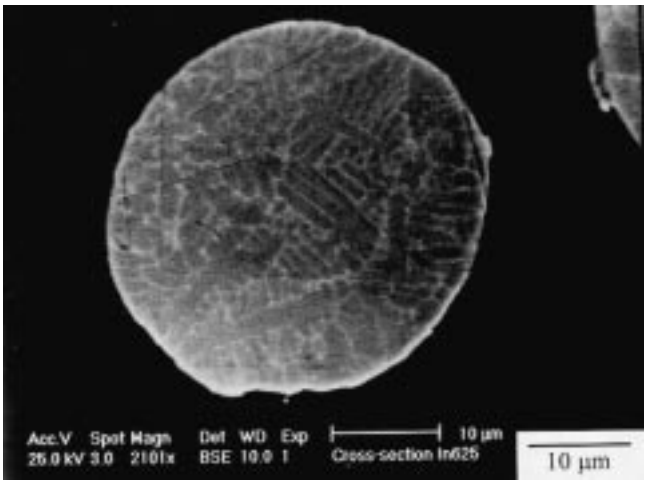

(b)

Fig. 4 SEM BSE images on the cross section of particles. Grains within particles are visible. **(a)** Equiaxed grains and **(b)** dendritic structure

there is no measurable difference in line broadening, *i.e.*, from defect substructure of chemical segregation,[18] as a function of particle size.

Neither endothermic nor exothermic peaks were observed on DTA curves of the as-received (M) powder until melting of the powder. This indicates that the powder does not experience any phase transformation prior to melting. The melting temperatures for the solidus and liquidus line were 1591 and 1663 K, respectively. These values are slightly higher than those in the published data, which give 1563 and 1623 K, respectively.[19]

Figure 4 shows SEM BSE images of the particle cross section, from which grains within particles are visible. Figure 4(a) exhibits equiaxed grains and Fig. 4(b) shows a dendritic structure. The cross-sectional microstructures of the particles were consistent with those on the external surfaces. However, the average grain size of the cross section measured from ten particles is 2.71 μm, while on external surfaces, it is only 1.83 μm.

The cross-sectional microhardness of the particles was tested using a load of 100 g. The average value was 258.6 HV_{100}.

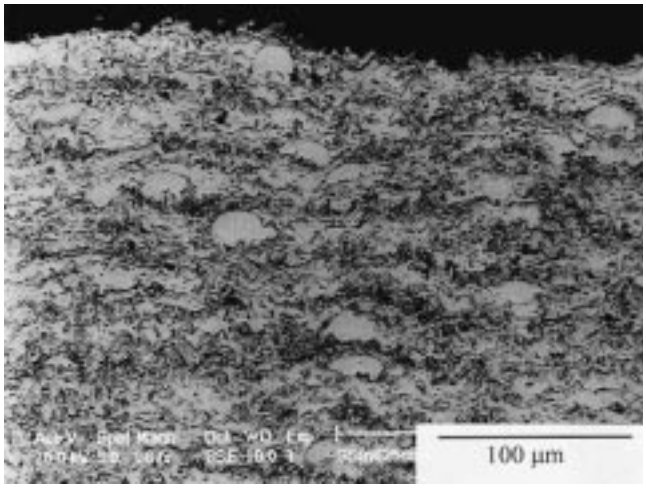

(a)

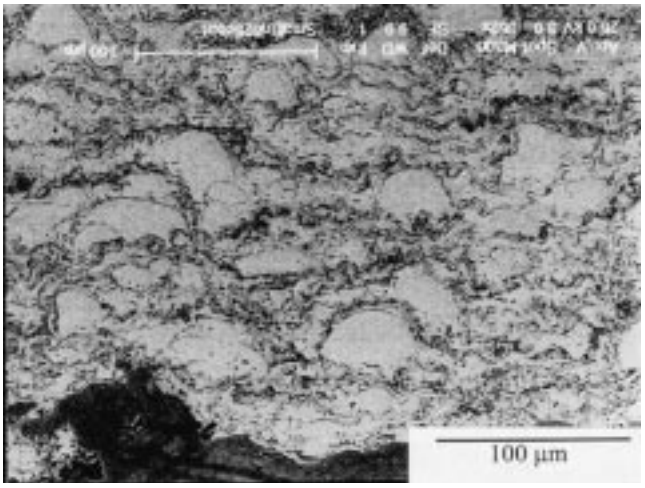

(b)

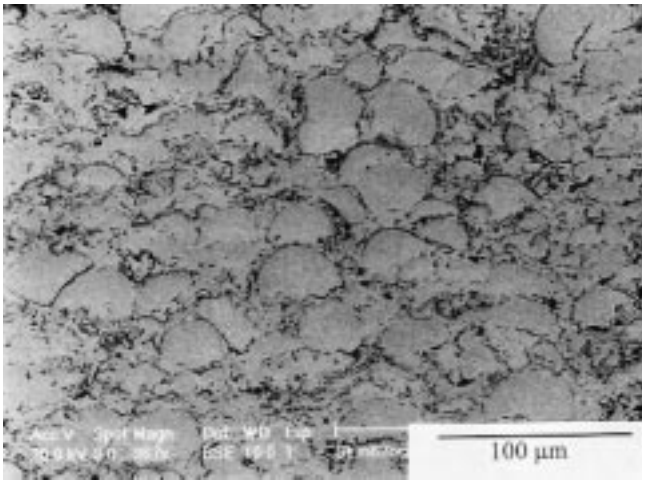

(c)

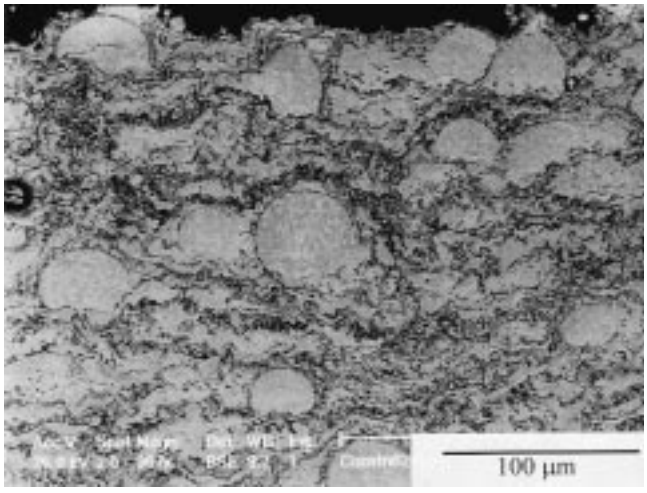

(d)

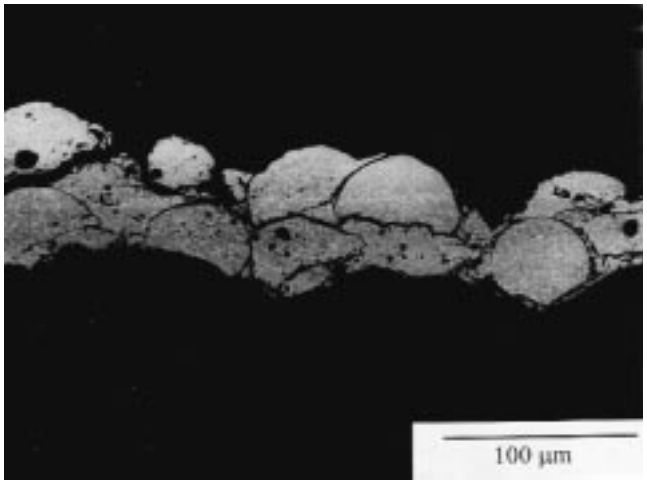

(e)

Fig. 5 SEM BSE images of the coating cross section. **(a)** SS coating, **(b)** S coating, **(c)** SL coating, **(d)** M coating, and **(e)** L coating

Table 4 Dependence of volume fraction and average chord of unmelted particle on the particle size of feedstock powder

Coating Code	SS	S	SL	M	L
Average particle diameter (μm)	17.01	26.71	36.02	44.96	69.97
Volume fraction (%)	4.9	12.9	54.8	19.5	. . .
Average chord (μm)	26.4	37.0	38.5	39.5	58.3

3.2 Microstructure of the Coatings

The SEM BSE images of the coatings made from different particle size powders are shown in Fig. 5. The designation S coating means that the coating was sprayed using the S powder, similarly with SS, SL, M, and L coatings. During spraying, all powders exhibited good flowability. The SS, SL, S, and M powders formed dense coatings; however, a complete L coating was not produced (Fig. 5e). It is noted that the volume fraction of unmelted particles is particle size dependent.

A large number of unmelted cross-sectional particles that appear to be near semicircular would be dome shaped in three-dimensional space. Some spherically shaped unmelted cross-sectional particles are also observed, which are shown in Fig. 5(d). During spraying, a large solid particle impacts onto the substrate, or already deposited layers, at a very high rate. The side that experiences the impact forces first deforms and spreads, and thus, a dome-shaped unmelted particle is formed. This process is discussed in more detail in Section 3.4. To describe the dimensions of the unmelted particles in the coatings, the average maximum chord of unmelted particles was statistically measured from 100 random particles. This average maximum chord, defined as the widest dimension of the unmelted particles, is slightly less than the average diameter of the particles in three-dimensional space. To that effect, it is important to make two observations. First, on the cross section of the coatings, the average maximum chord is less than or equal to the average diameter of the particles; Second, the average diameter of the cross-sectional particles (two dimensions) is less than that in three dimensions. Inspection of the published literature[20–23] shows that there are a large number of investigations dealing with the conversion from size distribution of particles on a two-dimensional plane to that in a three-dimensional space. The present methodology is intended to provide a comparison basis among the different coatings and, hence, not an accurate quantitative description of the powder characteristics. The volume fractions of unmelted particles are also measured and listed together with the average maximum chord in Table 4.

The volume fraction of the unmelted particles increases with increasing average particle size; however, it also closely depends on the particle size distribution. For example, there are many more unmelted particles in the SL coating, sprayed using the powder with an average particle diameter of 36.02 μm, than in the M coating sprayed using powder with average particle diameter of 44.96 μm. A detailed examination shows that most of the individual unmelted particles range between 30 and 50 μm. On the basis of data in Table 3 and Fig. 1, approximately 75% particles in the SL powder fall in the range of 30 to 50 μm, whereas approximately 25% of the particles in the M powder fall in the same size range. Therefore, the volume fraction of the unmelted particles in the coating depends on the amount of powder with a particle diameter ranging from 30 to 50 μm. The particles smaller than 30 μm mostly melt and play the role of a binder, while particles between 30 and 50 μm are embedded into this binder and remain as unmelted particles in the coatings. Under the same spraying condition, the average thicknesses of the SS, S, M, and SL coatings were measured to be 355, 353, 331, and 309 μm, respectively, and a complete L coating was not deposited. It is therefore thought that the particles larger than 50 μm fail to adhere to the substrate or already deposited layers. In the L powder, all particles are nearly larger than 30 μm; therefore, there is almost no binder phase and, consequently, most particles fail to adhere to the substrate. Therefore, a complete coating cannot be sprayed. In the SS powder, nearly all the particles are smaller than 30 μm, they melt completely during spraying, and only a few larger particles remain unmelted.

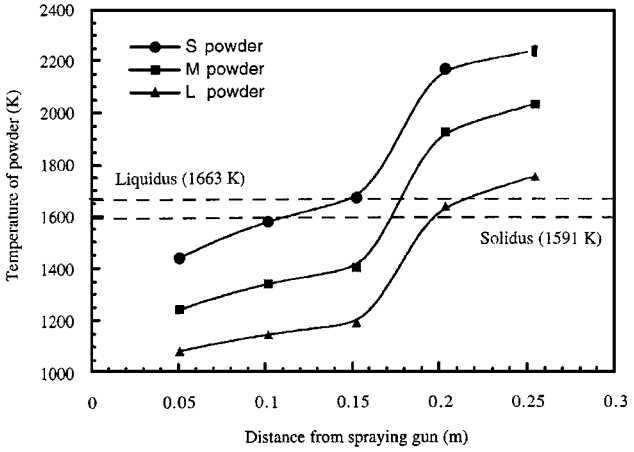

Fig. 6 Powder temperature profile in front of the spraying gun. The substrate was positioned at the site 0.203 m away from the spraying gun

During spraying, the melting of particles depends on the flame temperature and time interval which particles are exposed to that temperature. Using the "In-Flight" diagnostic equipment that accompanies the HVOF system, a quantitative investigation was conducted to find a relation between the particle temperature and spraying distance. This experiment was performed using the S, M and L powders, and the results are plotted in Fig. 6. The measured temperature values come from the average of 10 readings and the standard deviation of the measured temperature readings, which hence reflects repeatability of the measurements; the temperature ranges from ±4 to ±11 K, although the accuracy for absolute temperature measurement is 5% of the value according to the equipment specifications. The substrate was positioned a distance of 0.203 m away from the spraying gun. It was found that particle temperature increased with the decreasing particle size. The S powder underwent a maximum temperature of 2170 K, while the L powder experienced a maximum temperature of 1650 K; thus, adjusting particle size is an effective implementation to control the particle temperature. From this analysis, it is apparent that large particles did not melt during the spraying process, because the maximum temperature the large particles experienced was just over their melting temperature, with dwell time (flight time of particle during spraying) of only approximately 0.00067 s (assuming particle velocity was 300 m/s, Table 5).

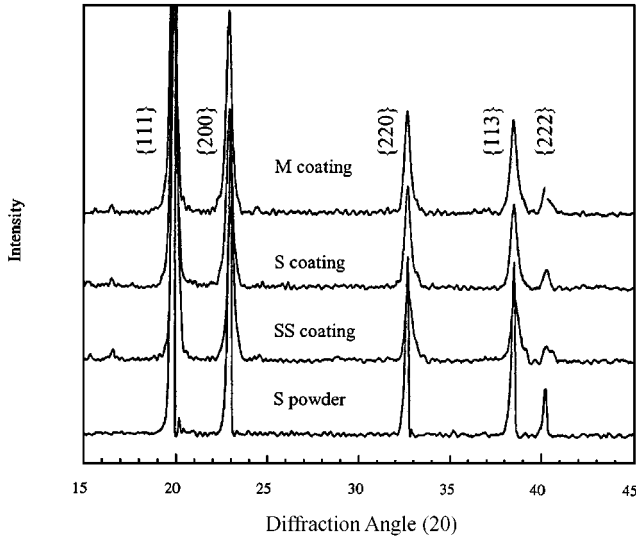

Fig. 7 XRD spectra of Inconel 625 coatings. As a comparison, the XRD spectra of the as-received powder (M powder) is also plotted again. XRD indicates that no new phase forms during sprayings.

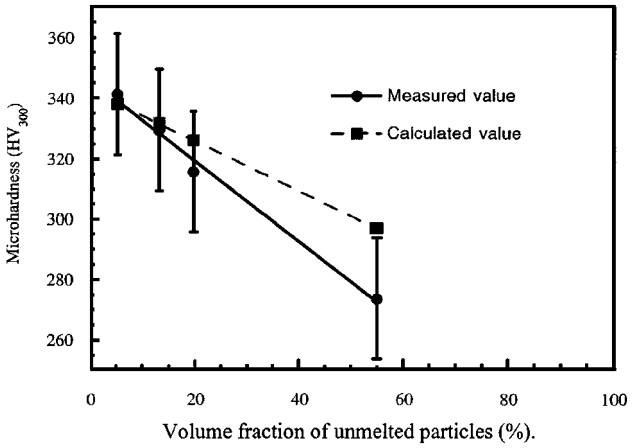

Fig. 8 Microhardness of the coatings as a function of volume fraction of the unmelted particles

Table 5 Influence of particle size on particle temperature and velocity of Inconel 718[3]

Particle size (μm)		14	16	19	22	26	31	38	44	53	62
IDJ1	Temperature (K)	2468	2464	2450	2416	2276	1939	1604	1533	1465	1418
	Velocity (m/s)	515	487	452	426	393	359	329	309	283	265
IDJ4	Temperature (K)	2840	2840	2842	2842	2834	2811	2738	2626	2347	1970
	Velocity (m/s)	554	523	479	448	412	378	345	323	297	276

Propylene produces 100 K higher temperature than hydrogen;[10] therefore, unmelted particles were not observed in Inconel 625 coatings sprayed using propylene as fuel.[2,10] By altering the fuel-oxygen ratio, the flame temperature changes. Compared to the fuel-oxygen ratio recommended by the gun manufacturer, Knight and Smith[15] found that a 20% increase in the fuel-oxygen ratio decreased the amount of unmelted particles in a NiCr coating. By contrast, a 20% decrease in the fuel-oxygen ratio decreased the degree of melting in the resultant coating. Using the "PROCESS" computer program, Varacalle *et al.*[3] conducted a modeling investigation of the HVOF process for gas-atomized Inconel 718 alloy using propylene as fuel. The effects those particle sizes have on particle temperature and velocity, at a stand-off distance of 0.203 m from the spray gun, are listed in Table 5. IDJ1 and IDJ4 are their experiment codes, indicating the fuel-oxygen ratios of 0.207 and 0.290, respectively.

The data in Table 5 indicate that particle temperature and velocity decrease as particle size increases. There is a 1000 K difference in particle temperature between 16 and 53 μm particles. In their simulation, predicted relations between particle temperature and spraying distance also appear similar to that of the present measured particle temperature profile (Fig. 6), although the present experiment used hydrogen as fuel with a fuel-oxygen ratio of 2.80.

3.3 Phase Constitution, Hardness, and Grain Size of the Coatings

The XRD spectra of the SS, S, and M coatings are shown in Fig. 7. Only one phase, the fcc structure, is identified in Fig. 7, although XRD peaks are noticeably broader. The full-width at half-maximum intensity values in XRD for {111}, {200}, {220}, {113}, and {222} planes were measured and the results are listed in Table 6.

It is observed that the XRD peaks evidently become broader with a decrease in the volume fraction of unmelted particles. The present results indicate that the grain size in unmelted particles is larger than 2 μm, as shown in Fig. 10, and the grain size in melted regions is approximately 500 nm (>>100 nm);[10] therefore, the broadening of XRD is presumably caused by microstrain.[18] Therefore, a more severe microstrain occurs in the coatings containing a low volume fraction of unmelted particles than in the coatings containing a high volume fraction of unmelted particles.

Edris *et al.*[10] found Cr_2O_3 and $NiCr_2O_4$ oxides in Inconel 625 coatings sprayed using HVOF with propylene. In their XRD measurements, a scanning rate of 1.5°/min was used. The present experiment was conducted with a scanning rate of 0.12°/min; therefore, the absence of oxide peaks in the present coatings may be attributed to the fact that their volume fraction is lower than the x-ray detection limit (usually, 5%). Increasing flame temperature can lead to the formation of oxide phases.[3,15] Knight and Smith[15] showed that a 20% increase in the fuel-oxygen ratio not only decreased the amount of unmelted particles in NiCr coating, but also increased the amount of oxide phases. By contrast, a 20% decrease in the fuel-oxygen ratio resulted in coatings with a lower degree of oxidation. Oxides were not detected in the coatings sprayed using hydrogen as fuel. In the Inconel 625 coatings sprayed by Edris *et al.*, unmelted particles were not found; this indicates that there was a very high flame

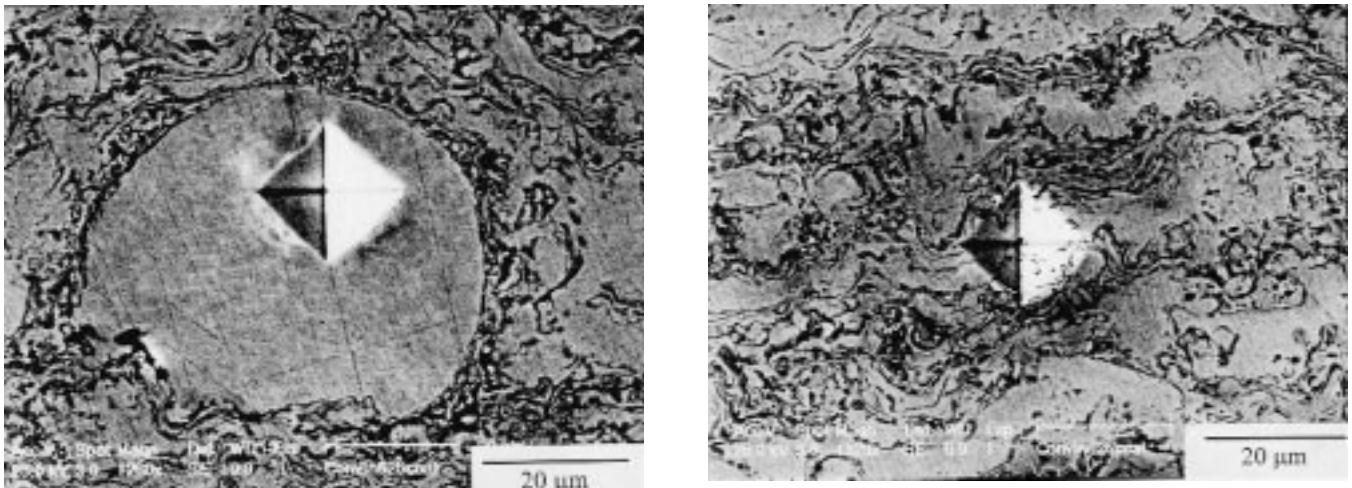

(a) **(b)**

Fig. 9 Microhardness indentations **(a)** in an unmelted particle and **(b)** in the matrix

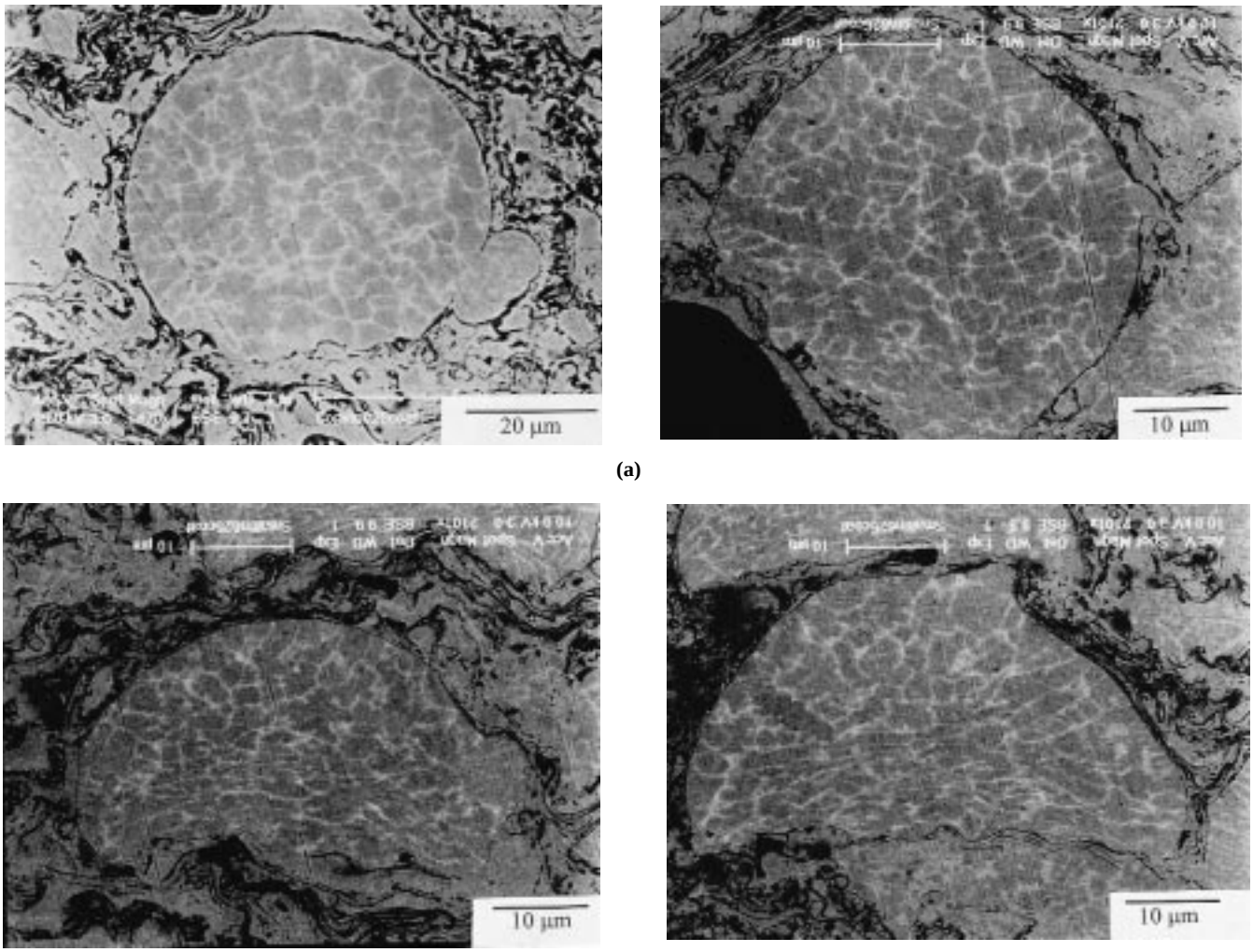

(a)

(b)

Fig. 10 SEM BSE images demonstrating grains in unmelted particles **(a)** near spherical unmelted particles and **(b)** dome-shaped unmelted particles

Table 6 Full-width of XRD peaks at the half of maximum intensity (degrees)

Materials	{111}	{200}	{220}	{113}	{222}
Powder	0.1874	0.1921	0.1932	0.2015	0.1935
M coating	0.2530	0.3374	0.3621	0.4031	0.2822
S coating	0.2588	0.3611	0.3598	0.4228	0.3528
SS coating	0.2855	0.3777	0.4338	0.5164	0.6059

temperature used during spraying. Therefore, the absence of oxides in the present coatings is attributed to the low flame temperature and use of hydrogen rather than propylene.

Figure 8 shows the microhardness of the coatings plotted as a function of volume fraction of the unmelted particles. It is apparent that microhardness decreases linearly with the increasing volume fraction of the unmelted particles. The microhardnesses of individual unmelted particles and the matrix were also measured using a load of 100 g and were found to be 259.3 and 342.3 HV_{100}, respectively. It is worth noting that the microhardness of the unmelted particles is nearly the same as that of the feedstock powder (258.6 HV_{100}). Indentations in an unmelted particle and in the matrix are shown in Fig. 9.

Using a simple rule-of-mixtures equation, $HV_c = V_u\, HV_u + V_m\, HV_m$, where HV_c is the microhardness of the coatings, V_u is volume fraction of the unmelted particles, $HV_u = 259.3$ is the microhardness of the unmelted particles, $V_m = 1 - V_u$ is volume fraction of the matrix, and $HV_m = 342.3$ is the microhardness of the matrix. The microhardness of the coatings was calculated and plotted in Fig. 8. In the case of low V_u, the calculated values approach the measured value; however, in the condition of high V_u, the measured microhardness is much lower than the calculated one. In the calculation associated with microhardness, the influence of the porosity and residual stresses in the coatings on the microhardness was not considered. However, in as-sprayed coatings, porosity and residual stresses are inevitable. The microhardness of a coating primarily depends on a combination of the volume fraction of unmelted particles, porosity, and residual stresses. The presence of porosity greatly leads to a decrease in microhardness. The coatings with low V_u are very dense, and thereby lack porosity. In contrast, to in the condition of high V_u, some porosity was found in the gaps among unmelted particles. The higher porosity in the coatings with high V_u is attributed to the lower particle temperature. Therefore, there is a greater decrease in microhardness, due to the presence of porosity, in the coatings with high V_u than those with low V_u. Residual stresses can cause an increase in microhardness. A greater broadening of XRD peaks, which is presumably caused by microstrain in the coatings, is observed in the coatings with low V_u than in those with high V_u. Thus, higher residual stresses exist in the coatings with low V_u than in those with high V_u. Consequently, contributions of residual stresses to microhardness in the coatings with low V_u are larger than those with high V_u. As the result of the analyses above, the microhardness of the coatings with low V_u approaches the corresponding calculated value, and in the condition of high V_u, the measured microhardness is much lower than the calculated one.

Figure 10 shows BSE images showing grains in unmelted particles. The average grain size is measured to be 2.83 μm, very close to that of the feedstock powders. In the near circular (spherical) unmelted particles, the morphology of the grains remains the same as that of feedstock powders. In the semicircular (dome shaped in three-dimensional space) unmelted particles, grains located at regions that are in contact with the substrate or already deposited layers are deformed along the direction parallel to the surface of the substrate. There is no evidence to indicate that grains also deform on the opposite side. Therefore, it is thought that spherical unmelted particles did not experience any change, and deformation occurred in the local region of the dome-shaped unmelted particles. The present results indicate that, under certain conditions, microstructure and properties of the feedstock powder can be maintained in coatings.

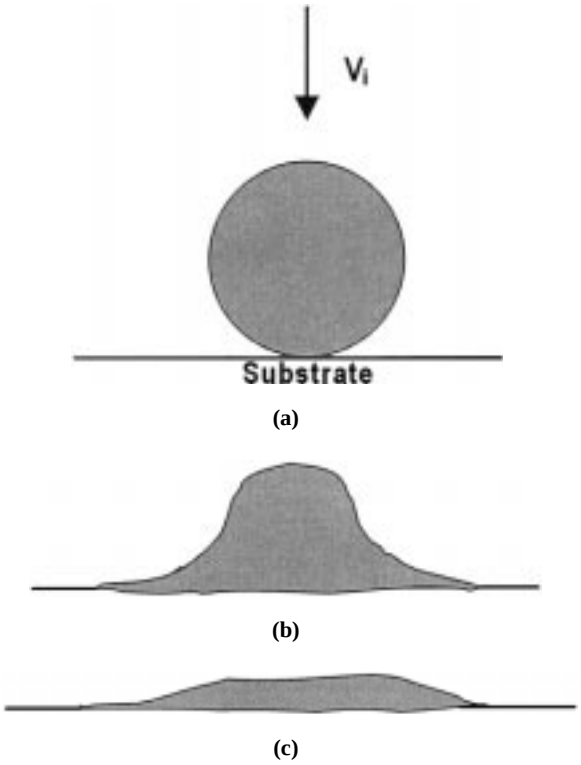

Fig. 11 A schematic of the droplet flattening mechanism.[25] **(a)** A droplet at velocity V_l impinges onto the substrate. **(b)** Spreading of droplet. **(c)** Solidifying of deformed droplet

3.4 A Lamellar Microstructure

The presence of unmelted particles in the coatings affects the formation of the lamellar microstructures that are typically observed in HVOF sprayed coatings.[1,2,10–15] A flattening mechanism was proposed to describe the formation of lamellar microstructures during spraying.[1,10,24–27] On the basis of this mechanism, the coatings are built up by molten droplets impacting on the substrate or already deposited layers, spreading, flattening, and solidifying. A schematic diagram showing a liquid particle flattening during impingement is shown in Fig. 11.[25] After the droplet impinges on the substrate, spreading of the splat is caused by liquid flow in the downward direction perpendicular to the substrate and in the radial direction along the surface. Results from numerical simulation studies show that the rate of droplet deformation is significantly larger than the solidification rate.[25–27] Accordingly, a lamellar microstructure is con-

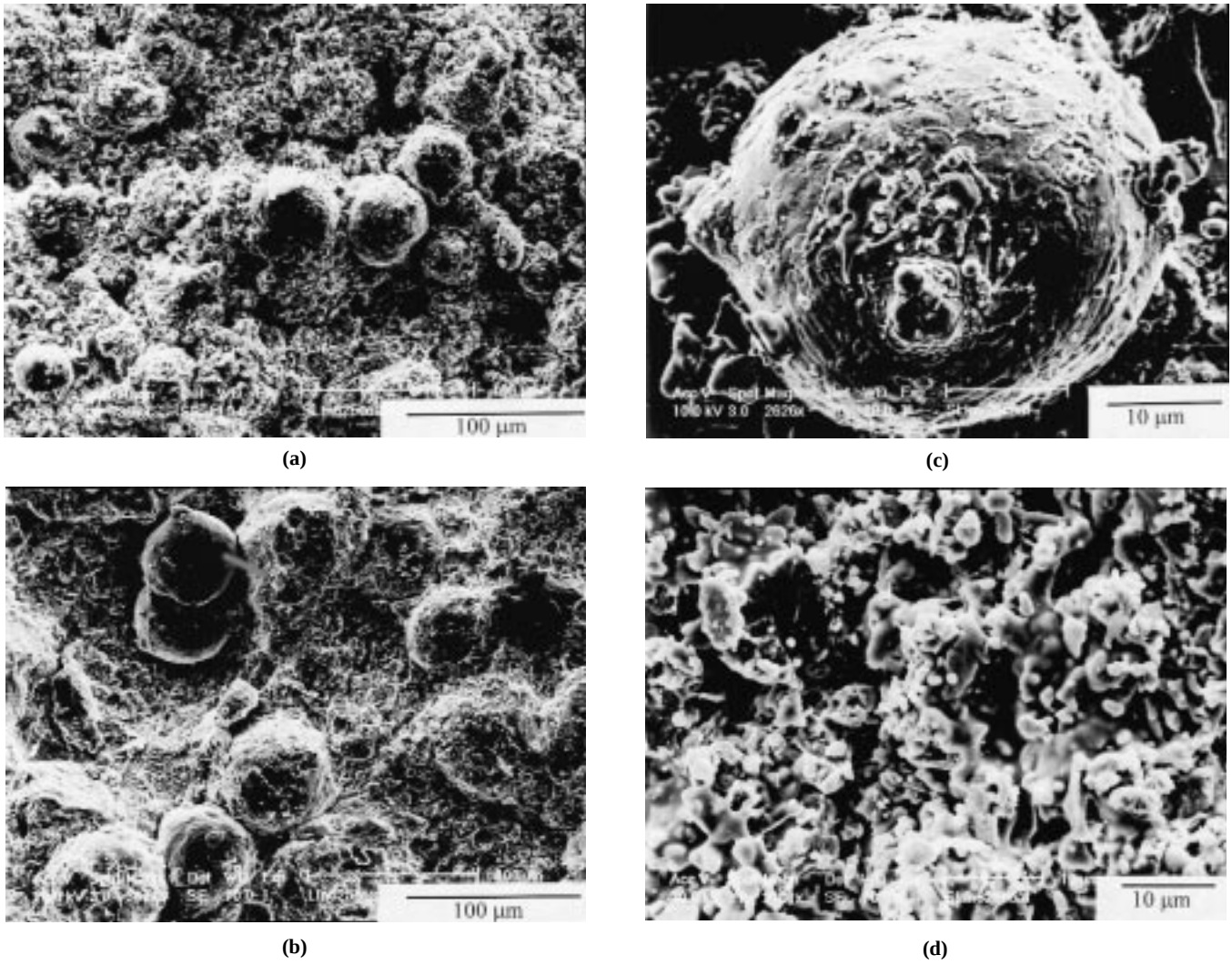

(a) **(c)**

(b) **(d)**

Fig. 12 SEM BSE images of the coatings on external surfaces. **(a)** SL coatings; **(b)** L coating; **(c)** a detailed view of an unmelted particle in the SL coating, and **(d)** magnification of a region in the matrix of the SL coating

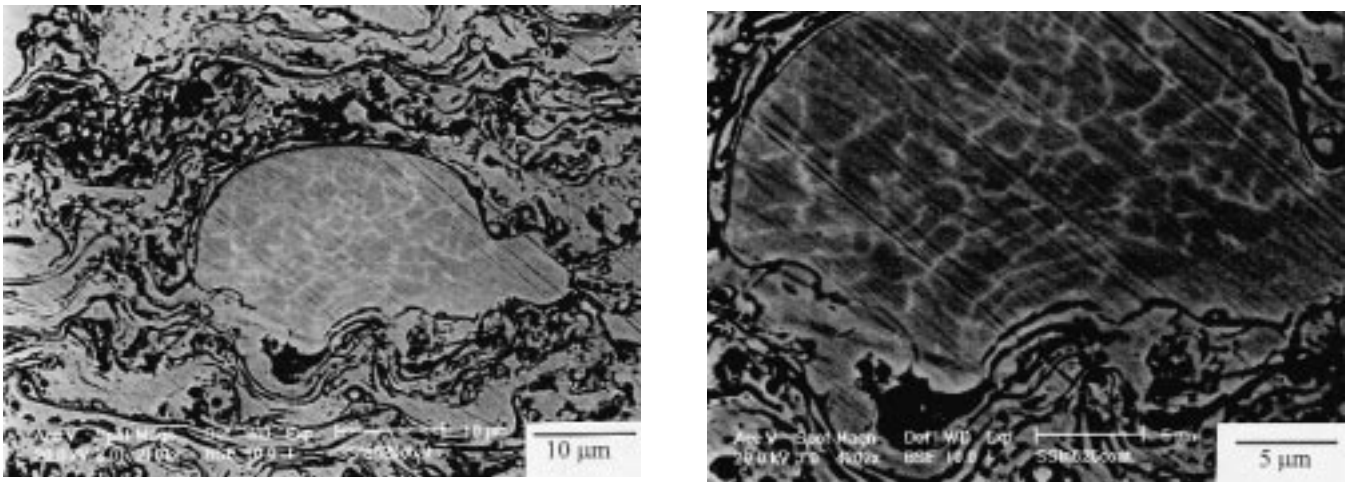

(a) **(b)**

Fig. 13 SEM BSE image illustrating discontinuities in microstructure near an unmelted particle. **(a)** An unmelted particle in lamellar microstructure and **(b)** magnification of (**a**)

sistently observed on cross sections of a coating. Figure 12 shows the surface of the SL and L coatings, in which a number of the unmelted particles are observed. When small molten droplets impact on a large unmelted particle, a flattening process occurs, see (Fig. 12c). However, the presence of an irregular surface on the already deposited layer affects the flattening behavior of the droplet, leading to microscopically irregular regions, as shown in Fig. 12(d). This is illustrated in Fig. 13, where the presence of an unmelted particle disrupts the lamellar microstructure and leads to discontinuities in the microstructure.

4. Conclusions

Using hydrogen as fuel and feedstock powders with different particle sizes, HVOF thermal-sprayed Inconel 625 coatings, containing unmelted particles, were synthesized. Powder characteristics and properties of the coatings were investigated using SEM, x-ray, and microhardness studies. The main results are briefly summarized as follows.

- The volume fraction of the unmelted particles in the coatings was dependent on the proportion of powder with a particle diameter in a particular range, in these experiments, 30 to 50 μm. This particle size range was primarily determined by the particle temperature during spraying.
- The particle temperature significantly decreased as particle size increased.
- The microhardness of the coatings containing unmelted particles could be predicted by a simple rule-of-mixtures equation for the case of a low volume fraction of unmelted particles. However, for the condition of a high volume fraction of unmelted particles, the measured microhardness is much lower than the calculated one, most likely due to the presence of porosity in voids occurring among unmelted particles.
- The microstructure and property of the feedstock powder could be retained in the corresponding coating under certain spray conditions. In these experiments, the microhardness of unmelted particles was very close to that of feedstock powder. Morphology and grains size in the near circular (spherical) unmelted particles remained the same as those of the feedstock powders. In the semicircular (dome shaped in three-dimensional space) unmelted particles, grains located at regions that are were in contact with the substrate or already deposited layers were elongated along the direction parallel to the surface of the substrate or already deposited layers. No evidence indicated that grains also deformed on the opposite side.

Acknowledgments

The authors gratefully acknowledge the financial support provided by the Office of Naval Research under Grant Nos. N00014-94-1-0017, N00014-97-1-0844, and N00014-98-1-0569.

References

1. L. Pawlowskia: *The Science and Engineering of Thermal Spray Coatings*, John Wiley & Sons, London, England, 1995.
2. M.D.F. Harvery, A.J. Sturgeon, F.J. Blunt, and S.B. Dunkerton: in *Thermal Spraying Current Status and Future Trends*, A. Ohmori, ed., High Temperature Society of Japan, Osaka, Japan, 1995, pp. 531-35.
3. D.J. Varacalle, Jr., M.G. Ortiz, C.S. Miller, A.J. Rotolico, J. Nerz, T.J. Steeper, and W.L. Riggs: in *Thermal Spraying: International Advances in Coatings Technology*, C.C. Berndt, ed., ASM International, Materials Park, OH, 1992, pp. 181-87.
4. O. Knotek and U. Schnaut: in *Thermal Spray: International Advances in Coatings Technology*, C.C. Berndt, ed., ASM International, Materials Park, OH, 1992, pp. 811-16.
5. S. Eidelman and X. Yang: *J. Thermal Spray Technol.*, 1996, vol. 5, pp. 175-84.
6. S. Eidelman and X. Yang: *NanoStructured Mater.*, 1997, vol. 9, pp. 79-84.
7. V.V. Sobolev and M. Guilemany: *Int. Mater. Rev.*, 1996, vol. 41, p. 13.
8. J.M. Guilemany, N. Llorca-Isern, M.D. Nunez, and J. de Paco: *Scripta Metall. Mater.*, 1994, vol. 31, pp. 1121-26.
9. J.M. Guilemany, J. Nutting, J.R. Miguel, and Z. Dong: *Scripta Metall. Mater.*, 1995, vol. 33, pp. 55-61.
10. H. Edris, D.G. Mccartney, and A.J. Strgeon: *J. Mater. Sci.*, 1997, vol. 32, pp. 863-72.
11. M.L. Lau, H.G. Jiang, W. Nuchter, and E.J. Lavernia: *Phys. Status Solidi (a)*, 1998, vol. 166, pp. 257-68.
12. E.J. Lavernia, M.L. Lau, and H.G. Jiang: in *Thermal Spray Processing of Nanocrystalline Materials, Nanostructured Materials*, G.M. Chow and N.I. Noskova, eds., Kluwer Academic Publishers, Dordrecht, The Netherlands, 1998, pp. 283-302.
13. J. He, M. Ice, S. Dallek, and E. J. Lavernia: *Metall. Mater. Trans. A*, 2000, vol. 31A, pp. 541-53.
14. J.He, M. Ice, and E.J. Lavernia: *Metall. Mater. Trans. A*, 2000, vol. 31A, pp. 555-64.
15. R. Knight and R.W. Smith: in *Thermal Spray: International Advances in Coatings Technology*, C.C. Berndt, ed., ASM International, Materials Park, OH, 1992, pp. 159-64.
16. T. Ueda, M. Sato, and T. Sugita: *J. Jpn. Soc. Prec. Eng.*, 1995, vol. 61, pp. 1448-52.
17. U.A. Tamburini, G. Campari, G. Spinolo, and P. Lupotto: *Rev. Sci. Instrum.*, 1995, vol. 66, pp. 5006-14.
18. H.P. Klug and L.E. Alexander: *X-ray Diffraction Procedures*, John Wiley & Sons, Inc., New York, NY, 1966, p. 138.
19. F.R. Morral: *Metals Handbook*, 9th ed., ASM, Metals Park, 1980, vol. 3, p. 216.
20. M.G. Kendall and P.A.P. Moran: *Geometrical Probability*, Charles Griffin, London, 1963.
21. R.T. DeHoll and F.H. Rhines: *Quantitative Microscopy*, McGraw-Hill, New York, NY, 1968.
22. S.A. Saltykov *Stereometric Metallography*, 3rd ed., State Publishing House for Metals and Sciences, Moscow, 1970.
23. E.E. Underwood: *Quantitative Stereology*, Addison-Wesley, Reading, MA, 1970.
24. C. Li, A. Ohmori, and Y. Harada: in *Thermal Spraying Current Status and Future Trends*, A. Ohmori, ed., High Temperature Society of Japan 1995, Osaka, Japan, pp. 333-39.
25. H. Maruo, Y. Hirata, and Y. Matsumoto: in *Thermal Spraying Current Status and Future Trends*, A. Ohmori, ed., High Temperature Society of Japan, Osaka, Japan, 1995, pp. 341-46.
26. M. Fukumoto, S. Katoh, and I. Okane: in *Thermal Spraying Current Status and Future Trends*, A. Ohmori, ed., High Temperature Society of Japan, Osaka, Japan, 1995, pp. 353-58.
27. O.P. Solonenko, A. Ohmori, S. Matsuno, and A. V. Smirnov: in *Thermal Spraying Current Status and Future Trends*, A. Ohmori, ed., High Temperature Society of Japan, Osaka, Japan, 1995, pp. 359-364.